



LAWRENCE
LIVERMORE
NATIONAL
LABORATORY

X-ray backlighter development at the National Ignition Facility (NIF)

M. A. Barrios, S. P. Regan, K. B. Fournier, R. Epstein, R. Smith, A. Lazicki, D. E. Fratanduono, J. Eggert, H. S. Park, C. Huntington, D. Bradley, G. W. Collins

June 19, 2014

Review of Scientific Instruments

Disclaimer

This document was prepared as an account of work sponsored by an agency of the United States government. Neither the United States government nor Lawrence Livermore National Security, LLC, nor any of their employees makes any warranty, expressed or implied, or assumes any legal liability or responsibility for the accuracy, completeness, or usefulness of any information, apparatus, product, or process disclosed, or represents that its use would not infringe privately owned rights. Reference herein to any specific commercial product, process, or service by trade name, trademark, manufacturer, or otherwise does not necessarily constitute or imply its endorsement, recommendation, or favoring by the United States government or Lawrence Livermore National Security, LLC. The views and opinions of authors expressed herein do not necessarily state or reflect those of the United States government or Lawrence Livermore National Security, LLC, and shall not be used for advertising or product endorsement purposes.

X-ray area backlighter development at the National Ignition Facility (NIF)^{a)}

M. A. Barrios^{1,b)}, S. P. Regan², K. B. Fournier¹, R. Epstein², R. Smith¹, A. Lazicki¹, R. Rygg¹, D. E. Fratanduono¹, J. Eggert¹, H.-S. Park¹, C. Huntington¹, D. K. Bradley¹, O. L. Landen¹, and G. W. Collins¹

¹Lawrence Livermore National Laboratory, Livermore, California, 94550, USA

²University of Rochester, Laboratory for Laser Energetics, Rochester, New York 14623, USA

(Presented XXXXX; received XXXXX; accepted XXXXX; published online XXXXX)

1-D spectral imaging was used to characterize the K-shell emission of $Z \approx 30$ -35 and $Z \approx 40$ -42 laser-irradiated foils at the National Ignition Facility (NIF). Foils were driven with up to 60 kJ of 3ω light, reaching laser irradiances on target between 0.5 to 20×10^{15} W/cm². Laser-to-X-ray conversion efficiency (CE) into the He $_{\alpha}$ line (plus satellite emission) of 1.0-1.5% and 0.15-0.2% was measured for $Z \approx 30$ -32 and $Z \approx 40$ -42 respectively. Measured CE into He $_{\alpha}$ (plus satellite emission) of Br ($Z=35$) compound foils (either KBr or RbBr) ranged between 0.16 -0.29%. Measured spectra are compared with 1-D non-LTE atomic kinetic and radiation transport simulations, providing a fast and accurate predictive capability.

I. INTRODUCTION

In inertial confinement fusion (ICF) experiments at the National Ignition Facility (NIF)¹, deuterium-tritium (DT) filled spherical capsules are imploded by a temporally tailored x-ray drive, generated by laser heating of the inner wall of a high- Z hohlraum. To achieve ignition, the DT fuel must be driven to high convergence (35-40)^{2,3}, resulting in the formation of a central hot spot with temperature > 5 keV and areal density > 0.3 g/cm². Reaching these conditions relies on the formation of a highly symmetric implosion. Previously only the shape of the x-ray self-emission was used to evaluate the symmetry of the implosion, assuming a direct correlation between the compressed fuel and self-emission shape. However recent simulation studies show it is equally important to mitigate/correct implosion asymmetries earlier in time; correcting low-mode asymmetries of the self-emission alone does not fully recover losses in yield.³

Low-mode asymmetries after the launch of the last shock and stagnation are measured through 2D-backlit X-ray radiography of the imploding shell.⁴ Previous backlighter (BL) work optimized the generation of x-ray flux for Zn and Ge foils under experimental constraints of the 2D-backlit radiography platform.⁵ This has enabled in-flight-shell symmetry and shell-velocity measurements for times between ~ 600 -300 ps before x-ray bang time, corresponding to shell radii of ~ 250 -140 μm .⁴ Late time measurements with the current platform are limited by the degrading contrast in the images (using a Ge BL with dominant x-ray emission at Ge He $_{\alpha}$ = 10.3 keV), as the shell reaches increasingly higher areal densities, and the onset of self-emission from the hot spot that degrades the data, making it challenging to determine accurately the location of the capsule limb. To radiograph higher areal density conditions in the shell, and measure in-flight shape symmetry at shell radii of ~ 100 μm where shape swings are predicted by simulations, higher photon energies are needed, requiring the development of higher Z backlighters.

Results presented here are a continuation of previous work on backlighter development on NIF,⁵ characterizing the K-shell emission of laser irradiated backlighter foils with atomic numbers varying from 30-42, corresponding to He $_{\alpha}$ line emission from 8.99-18.0 keV. For materials with $Z \geq 40$, measurements at NIF are the first reported. Optimizing K-shell x-ray flux for various foils has mostly been an empirical task. Having tools that provide a fast and accurate predictive capability will greatly benefit efforts toward improving backlighter performance. This would enable testing a wider range of laser parameters tailored for specific experimental considerations, such as required photon energy, photon flux of the main emission line, source size, temporal duration, and other experimental constraints. Predicted spectra generated using 1-D non-LTE atomic physics simulations are presented and compared with data collected at NIF. 1-D simulated spectra are shown to have enough accuracy (\sim factors of 2-5 between data and simulation) to be used as a fast predictive tool for mid- Z foils.

II. EXPERIMENTAL CONFIGURATION

Foils were driven with 4 or 8 NIF¹ beams delivering between 16-60 kJ of 3ω light on target, leading to laser irradiances between 0.5×10^{15} to 20×10^{15} W/cm². Beams were incident on the foil at 40° relative to the target normal. The laser beams profiles were smoothed using continuous phase plates⁶, forming either a (0.8 mm x 1.2 mm) elliptical spot or a 400 μm diameter circular spot at normal incidence. A subset of experiments used beams at best focus with no phase plates, leading to ~ 150 μm circular spot size. The main laser drive was a 2-5 ns square pulse that heated an underdense pre-formed plasma, generated by a 1 ns laser picket pulse 3 ns prior to the main laser drive arrival. Previous work has shown an increase in conversion efficiency (CE) is achieved by using a pre-pulsed foil, as the underdense plasma enables better coupling of the laser energy into thermal energy via inverse bremsstrahlung.^{7,8} Picket strength and delay time between picket and main drive were chosen based on previous work by Babonneau *et al.*⁹ with Ge. Foils were either (3 mm x 3

^{a)}Invited paper published as part of the Proceedings of the 20th Topical Conference on High-Temperature Plasma Diagnostics, Atlanta, Georgia, June, 2014.

^{b)}Correspondence should be addressed to: barriosgarci1@llnl.gov

mm) or (1 mm x 1 mm), with thicknesses ranging between 10-15 μm .

Absolute time integrated 1-D spectral images were obtained using Supersnout II (SSII), a four channel elliptically bent PET Bragg crystal spectrometer.¹⁰ The four independent energy channels of SSII were designed to measure x-ray emission from 6-16 keV, with overlapping energy ranges among the channels, recorded onto an SR image plate. Absolute measurements result from applying the measured integrated reflectivity of the elliptically bent PET crystals (first-order Bragg reflection),¹¹ the calibrated fade correction and sensitivity of the SR image plate,¹² and measured transmission of filters through the system. Resulting 1D-spectral images have 100 μm spatial resolution. K-shell emission from Zn, Ge, RbBr, and KBr foils were recorded in first-order Bragg reflection using SSII.

An *in situ* calibration of the second-order Bragg reflection of SSII PET crystals was achieved using data taken for a Kr K-shell gas pipe¹³, driven with 700 kJ at NIF. SSII measured Kr He_α and He_β line emission in first-order Bragg reflection in its highest energy channel (9.3-16.5 keV), and in second-order Bragg reflection in the remaining lower-energy channels. Data show the second-order Bragg reflection is ~ 50 -100 times weaker than the first-order Bragg reflection. Previous integrated reflectivity data for flat PET crystals show second-order integrated reflectivity is $\sim 20\text{X}$ weaker compared to first-order reflections.¹⁴ The larger difference in second and first-order crystal reflectivity for SSII is likely due to the mosaic structure in

the cleaved crystals. It is assumed here that the first and second-order integrated reflectivity of the curved PET crystals vary slowly such that calibration values can be applied to energies above 15.4 keV (Kr He_β). This *in situ* calibration of SSII crystals extends the upper limit of its spectral range to 25 keV, enabling measurement of K-shell emission for Zr, Nb, and Mo foils in second-order Bragg reflection. For these experiments filter designs that heavily attenuated first-order light, while transmitting enough second-order reflected light to yield detectable PSL signal levels on the image plate, were used. The current second-order calibration is limited to integrated X-ray yields. However, the background subtracted un-calibrated (PSL/px) line profiles can be scaled such that the integrated X-ray yield under the curve matches the absolute yield, derived from the second-order calibration, leading an absolute spectrum (J/keV/sr) as a function of photon energy.

SSII viewed the target emission either edge-on (most shots) or parallel to the target normal (small subset). FIG. 1 show typical 1-D spectral images and the resulting spectrum recorded using SSII in (a) first-order and (b) second-order Bragg reflection, for a Zn (15 μm thick) and Mo (12.5 μm thick) foil respectively. FIG. 1 shows good agreement in both absolute yield and line emission shapes between the four independently calibrated channels. Variation in the integrated yields between channels is typically between 10-20%.

III. MEASURED RESULTS

Laser-to-X-ray conversion efficiency into He_α was measured for Zn (15 μm , green diamonds), Ge (10-12 μm on 200 μm graphite substrate, orange squares), RbBr (10-12 μm on 25 μm Al substrate, Br-upright magenta triangles, Rb-downward pointing triangle), KBr (10-12 μm on 25 μm Al substrate, upright magenta triangles), Zr (7 μm , blue circles), Nb (12 μm , black stars), and Mo (12.5 μm , cyan rectangle) foils, and is plotted in FIG. 2 as a function of peak laser irradiance. For each experiment x-ray yield is obtained by integrating the absolute brightness (J/keV/sr) for each SSII channel that measures the He_α line plus satellite emission from each element under consideration, after subtraction of a local continuum $I_0 e^{-h\nu/kT}$. Data in FIG. 2 correspond to the average value and standard deviation among

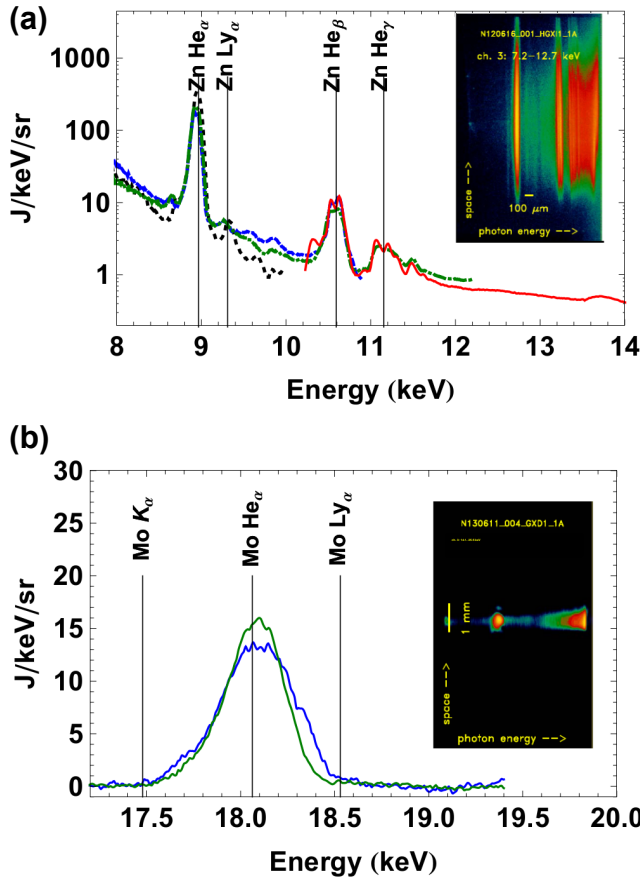


FIG. 1. (Color online) 1-D spectral image from one of the channels of SSII and resulting time-integrated spectrum for (a) first-order Bragg reflection for a Zn foil and (b) second-order Bragg reflection for a Mo foil. Data show good agreement between the independently calibrated spectral channels.

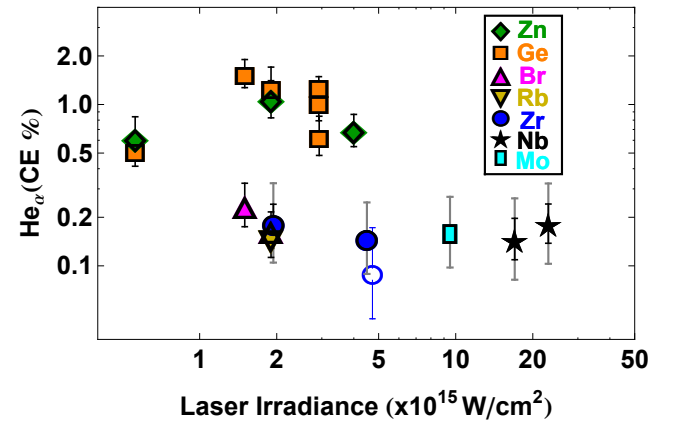


FIG. 2. (Color online) Measured laser-to-X-ray conversion efficiency into He_α plus satellite emission, using SSII, for Zn (green diamonds), Ge (orange squares), Br (magenta upright triangles), Rb (yellow downward triangle), Zr (blue circles; open circle: no pre-pulse), Nb (black stars), and Mo (cyan rectangle) targets.

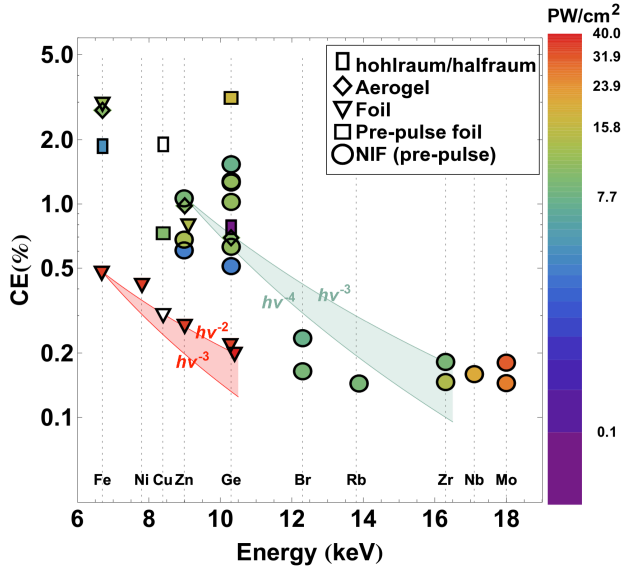


FIG. 3. (Color online) Measured conversion efficiency as a function of material He_α , where symbol color represents experiment laser irradiance, as indicated by color bar.

the channels measuring the line emission. For second-order Bragg reflected measurements, the gray error bar correspond to the total uncertainty, which is the quadrature sum of the statistical variations between channels and additional systematic error due to uncertainties in the second-order calibration. Filled (open) symbols represent pre-pulsed (no pre-pulse) experiments. Based on data trends, peak CE for Zn and Ge occur around $1.0\text{--}1.5 \times 10^{15} \text{ W/cm}^2$; Maximum CE into He_α measured in this study for Zn and Ge was $(1.1 \pm 0.3)\%$ and $(1.5 \pm 0.3)\%$ respectively. All but one shot for Ge used one-sided laser irradiation. A 30% increase in the CE into Ge He_α was observed between one-sided, $(1.0 \pm 0.3)\%$, and two-sided, $(1.3 \pm 0.2)\%$, foil irradiation, at $2.9 \times 10^{15} \text{ W/cm}^2$. Compound Br films (KBr and RbBr) yielded significantly lower CE into Br He_α than Zn and Ge foils at similar laser irradiances. Peak CE measured into Br and Rb He_α was $(0.23 \pm 0.07)\%$ and $(0.15 \pm 0.04)\%$. This sharp decrease in He_α x-ray production is likely a consequence of having less emitters per unit area in the case of the Br compound foils. Three shots were taken with Zr foils, two using a pre-pulse and one without a pre-pulse. Measured CE varied little between pre-pulsed foils driven to laser irradiances of 1.94 and $4.5 \times 10^{15} \text{ W/cm}^2$, measuring $(0.18 \pm 0.1)\%$ and $(0.15 \pm 0.07)\%$. Using only a main laser drive on a $15 \mu\text{m}$ Zr foil at $4.7 \times 10^{15} \text{ W/cm}^2$ resulted in a reduced CE of $(0.09 \pm 0.05)\%$. The Nb and Mo foils produced similar x-ray yields than Zr. CE into Nb He_α of $(0.15 \pm 0.09)\%$ and $(0.18 \pm 0.1)\%$, for laser irradiances of 1.7 and $2.3 \times 10^{16} \text{ W/cm}^2$. The recorded CE of Mo at $9.5 \times 10^{15} \text{ W/cm}^2$ was $(0.16 \pm 0.08)\%$.

FIG. 3 compares CE measurements performed by other studies using a variety of different platforms, hohlraums/halfraums^{15,16}: rectangles, aerogels^{17,18}: diamonds, no pre-pulse foils^{19–21}: downward triangles, pre-pulsed foils other studies^{9,22,23}: squares, and pre-pulsed foil data measured at NIF: circles, as a function of material He_α line emission. In this figure the color of the symbols represents the laser irradiance used for a particular data point, referenced to the color bar on the right of the graphic. Pre-pulsed data at NIF yielded higher CE than previous data using aerogels, hohlraums/halfraums, and no pre-pulsed foils. Previous work by Workman *et al.*^{19,20} carefully

studied the scaling of CE with material Z , reporting Z -scaling consistent with $(h\nu)^{-2}$ to $(h\nu)^{-3}$, as shown by the red bounds in FIG. 3. Pre-pulsed data at NIF show Z -scaling consistent with previous result from other types of targets, consistent with $(h\nu)^{-3}$ to $(h\nu)^{-4}$. In this plot the under performance of the Br compound films is more evident, where measured CE into He_α is $\sim 2X$ less compared to the green scaling curve. Again, this can be expected since these films had $\sim 2X$ less atoms of each type.

IV. K-SHELL EMISSION SPECTRA SIMULATIONS

A fast and accurate predictive capability for K-shell emission of laser driven foils was developed by coupling the 1D Lagrangian hydrodynamics code, LILAC²⁴, with an atomic physics post-processor code, SPECT3D²⁵. SPECT3D²⁵ is a collisional-radiative atomic physics code that calculates the spectral emission for elements with $Z \leq 36$, for given T_e and n_e conditions, by solving the radiative transfer equation along discrete lines of sight. The spectral model in SPECT3D²⁵ includes collisional and radiative excitations and decays, radiative recombination, autoionization, and dielectronic recombination.

The laser pulse shape, spot size, and energy delivered on target were used in LILAC to simulate the time dependent plasma conditions (T_e , n_e) reached by the laser-driven foil. For planar simulations, where no divergence effects are included, the average irradiance within the beam spot size was modeled in LILAC²⁴ in planar geometry. To include plasma divergence effects 1-D spherical simulations were performed, using a spherical surface area four times larger than the beam spot size. For backlighter emission simulations, SPECT3D was used with detailed-configuration-accounting (DCA) models with atomic level populations computed assuming non-local thermodynamic equilibrium (non-LTE). The radiation transport was calculated with either local or non-local coupling to the atomic level rate equations. In the first

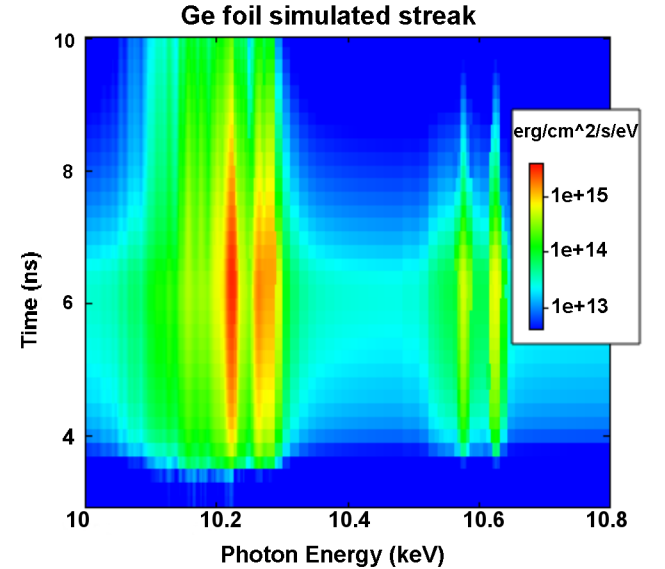


FIG. 4. (Color Online) Simulated streak image using LILAC²⁴ and SPECT3D²⁵, with local radiation transport, for a Ge foil driven with peak laser irradiance of $1.9 \times 10^{15} \text{ W/cm}^2$. Simulation shows generation of Ge He_α emission closely follows the laser main drive that starts and ends at ~ 3.4 ns and 6.4 ns, respectively.

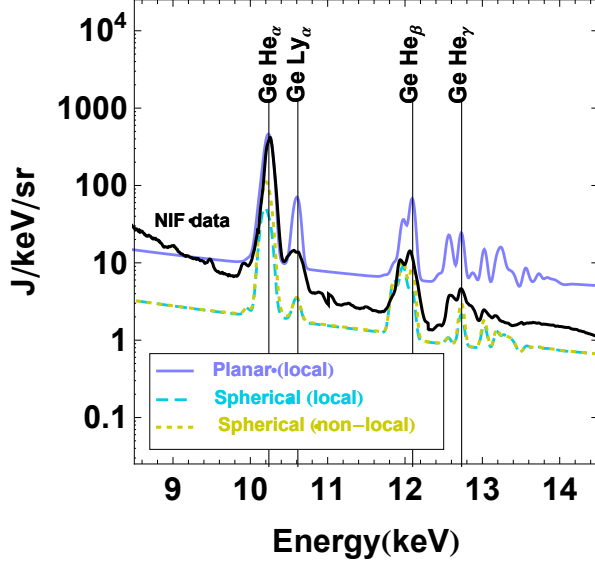


FIG. 5. (Color Online) Measured spectra using SSII (solid black) is compared to 1-D spectral simulations corresponding to planar (solid purple) and spherical (dashed blue) simulations with local escape factors, and spherical simulation using non-local radiation transport (dotted yellow).

case the local escape probability is calculated for each transition and is applied to the rate equation, in the latter case the photon absorption rates, which correspond to non-local effects, are calculated in addition to the local escape probability, and used in the rate equation. Additionally SPECT3D has the capability of calculating several independent simulation times corresponding to results from hydro-codes (time-independent), where calculations progress between quasi-static states, or computing the solution of time-dependent atomic rate equations, where the time-dependent conditions of the hydro-code are applied (time-dependent). For backlighter simulations little difference was observed between time-dependent and time-independent calculations, therefore all spectral simulations presented here were evaluated using time-dependent rate equations.

The simulated temperature and density gradients predicted by LILAC were post-processed using SPECT3D to characterize the K-shell plasma emission as a function of time, resulting in a simulated spectral streak for a Ge foil, as shown in FIG. 4. This simulation corresponds to a 12 μm Ge foil driven with 50 kJ of 3 ω light using a nominally 2 ns square pulse, used as the main drive, arriving 3 ns after a 1 ns pre-pulse. The resulting peak laser irradiance on target was $1.9 \times 10^{15} \text{ W/cm}^2$. The simulation in FIG. 4 shows generation of Ge K-shell emission soon after the main laser drive is fired at ~ 3.5 ns. The He_α emission peaks at ~ 6.2 ns, close to the end of the main laser drive, and quickly decays as the drive turns off. To enable comparison with measured data recorded using SSII, the simulated streak was integrated in time.

Three types of simulations were run for various as-shot conditions for Ge foils: planar and spherical simulations with the effects of local photon-escape factors, and spherical simulations with non-local photon transport and escape. Data, solid black curve, and simulation results are compared in FIG. 5, showing measured spectra is bounded between spherical (local: dashed blue, non-local: dotted yellow) and planar (local: solid purple) simulations. Including divergence effects decreases the x-ray continuum level by $\sim 5X$, with little change to the slope of the continuum. FIG. 5 shows line emission into Ge He_α and Ge Ly_α

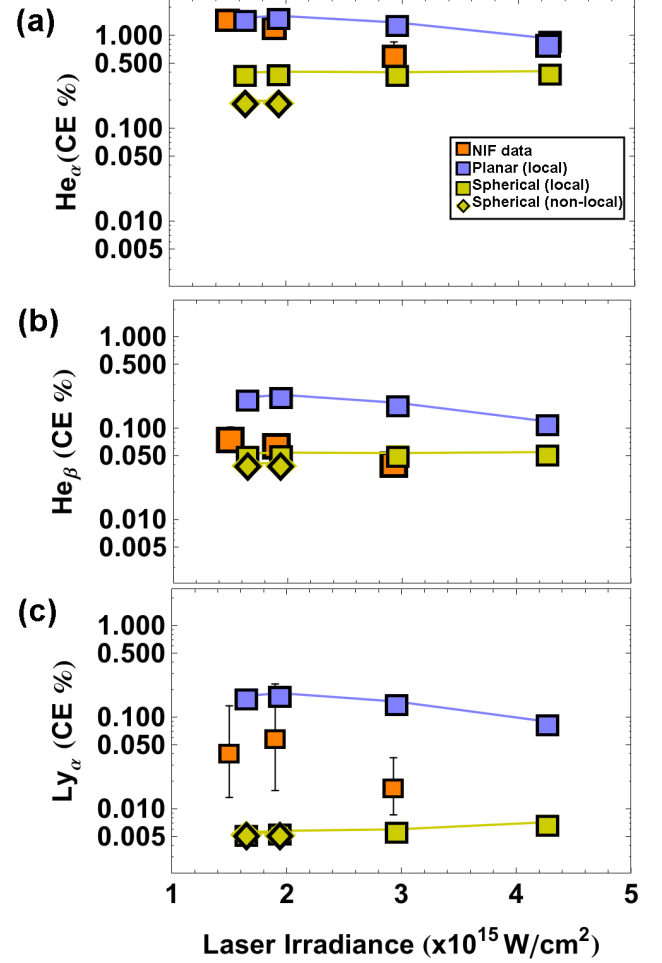


FIG. 6. (Color Online) Predicted laser-to-x-ray conversion efficiency (CE) into Ge (a) He_α , (b) He_β , and (c) Ly_α line plus satellite emission from 1-D planar and spherical simulations bounds measured CE using SSII.

are influenced by including divergence effects, where the line emission peak x-ray yield decreases by a factor of 10 and 20, respectively, between planar and spherical simulations assuming local radiation transport. Including non-local radiation effects for spherical simulations has little effect on the x-ray continuum, but does influence the total X-ray yield into a particular line emission as well as the line shape, which is dictated by the excitation of the main line and its satellite states.

Measured CE into line plus satellite emission of the Ge He_α , He_β , and Ly_α emission lines was compared with simulation results after subtraction of the local x-ray continuum for various laser irradiances, as depicted in FIG. 6. Here all measured data are shown as the orange squares, planar and spherical simulations with local escape factors as the purple and yellow squares, respectively, and spherical simulations with non-local escape factors as the yellow diamonds. As shown in FIG. 6 (a) the measured CE (%) into Ge He_α is in close agreement with planar (local) simulations at laser irradiances below $2 \times 10^{15} \text{ W/cm}^2$, but in better agreement with spherical simulations at laser irradiances above that. CE into Ge He_α for planar (local) and spherical (local) simulations vary by a factor of four at lower irradiances, which reduces to a factor of two for higher irradiances. This trend between planar and spherical simulations, where larger

discrepancies occur at lower laser irradiance, is likewise evident in predicted x-ray yields into He_β and Ly_α line emission. Such trend could be a consequence of the spatial location where most of the Ge He_α occurs, as calculated by the simulations, where at lower irradiances the emission is closer in to the target surface and thus divergence effects have a larger influence. The measured CE into Ge He_β (FIG. 6 (b)) is better represented by the spherical simulations for all laser irradiances, while the Ly_α , much like the He_α plus satellite emission, is in closer agreement with planar simulations below $2 \times 10^{15} \text{ W/cm}^2$. Simulation results indicate that inclusion of non-local radiation effects has little to no effect on the resulting estimated yield into Ge He_β and Ly_α emission, but does decrease the calculated yield into the Ge He_α plus satellite emission by a factor of two. It is important to note that although these quick 1-D simulations do not always match the measured data, it is encouraging they adequately provide upper and lower bounds that could be used as a method of testing various laser configurations (changes in pre-pulse strength, delay time between pre-pulse and main drive, peak laser irradiance, etc.), to determine plasma conditions that optimize the production of He_α plus satellite emission for a given material. The resulting uncertainty in predicted x-ray yield between planar and spherical simulations is sufficient to provide photometric estimates for time-integrated measurements, but use of this platform for time-resolved diagnostics will require smaller variation between measured data and predicted signals. This current simulation platform can be further optimized by varying the effective spot size used in LILAC²⁴ simulations to empirically match measured data. Lastly, this platform can be extended to materials with Z higher than 36 by extending the spectral database SPECT3D typically uses.

V. CONCLUSIONS

Laser to X-ray conversion efficiency into He_α plus satellite emission of Zn, Ge, Br, Rb, Zr, Mo, and Nb was measured for pre-pulsed foils designed for x-ray area backlighting at the NIF. Laser irradiances on target over the range of $0.5\text{--}20 \times 10^{15} \text{ W/cm}^2$, achieved by varying the laser energy between 16–60 kJ, delivered in a 2–4 ns square pulse main drive with a picket 3 ns prior, with either (0.8 mm x 1.2 mm) elliptical, 400 μm diameter circular, or 150 μm diameter circular beam spot sizes. Foils investigated ranged in Z from 30 to 42. CE(%) was measured to be at or above 1% for Zn and Ge. The CE(%) of Br, Rb, Zr, Nb, and Mo were all close to ~0.2% for all laser irradiances. The latter high-Z foils can likely be further optimized by better tailoring the pulse shape used to drive them.

A fast and accurate (~ factors of 2–5 between data and simulation) predictive capability was developed for mid-Z foils, and compared to measured Ge data. The current platform using 1-D hydro simulations coupled to an atomic physics code is able to bound the measured backlighter spectral brightness. Future efforts will work toward better matching the spectral simulations to data, and extending the platform to produce spectra for materials with $Z > 36$.

Characterizing the He_α line emission of Zn and Ge backlighters was used to develop the current implosion radiography platform used at NIF. Extending measurements to materials with higher atomic number ($Z \approx 40\text{--}42$) now opens the possibility of radiographing higher density material. Using measured CE from the laser-irradiated Mo foil shows radiography measurements up to ~100 μm can be achieved.

ACKNOWLEDGEMENTS

The authors would like to thank the members of the NIF operations team for their support and effort for these experiments. This work was done under the auspices of the U.S. Department of Energy by Lawrence Livermore National Laboratory under Contract DE-AC52-07NA27344.

- ¹ G.H. Miller, E.I. Moses, and C.R. Wuest, Nucl. Fusion **44**, (2004).
- ² R.P.J. Town, D.K. Bradley, A. Kritcher, O.S. Jones, J.R. Rygg, R. Tommasini, M. Barrios, L.R. Benedetti, L.F.B. Hopkins, P.M. Celliers, T. Döppner, E.L. Dewald, D.C. Eder, J.E. Field, S.M. Glenn, N. Izumi, S.W. Haan, S.F. Khan, J.L. Kline, G.A. Kyralla, T. Ma, J.L. Milovich, J.D. Moody, S.R. Nagel, A. Pak, J.L. Peterson, H.F. Robey, J.S. Ross, R.H.H. Scott, B.K. Spears, M.J. Edwards, J.D. Kilkenny, and O.L. Landen, Phys. Plasmas 1994–Present **21**, 056313 (2014).
- ³ A.L. Kritcher, R. Town, D. Bradley, D. Clark, B. Spears, O. Jones, S. Haan, P.T. Springer, J. Lindl, R.H.H. Scott, D. Callahan, M.J. Edwards, and O.L. Landen, Phys. Plasmas 1994–Present **21**, 042708 (2014).
- ⁴ J.R. Rygg, O.S. Jones, J.E. Field, M.A. Barrios, L.R. Benedetti, G.W. Collins, D.C. Eder, M.J. Edwards, J.L. Kline, J.J. Kroll, O.L. Landen, T. Ma, A. Pak, J.L. Peterson, K. Raman, R.P.J. Town, and D.K. Bradley, Phys. Rev. Lett. **112**, 195001 (2014).
- ⁵ M.A. Barrios, K.B. Fournier, S.P. Regan, O. Landen, M. May, Y.P. Opachich, K. Widmann, D.K. Bradley, and G.W. Collins, High Energy Density Phys. **9**, 626 (2013).
- ⁶ S.N. Dixit, M.D. Feit, M.D. Perry, and H.T. Powell, Opt. Lett. **21**, 1715 (1996).
- ⁷ C.A. Back, J. Davis, J. Grun, L.J. Suter, O.L. Landen, W.W. Hsing, and M.C. Miller, Phys. Plasmas **10**, 2047 (2003).
- ⁸ C.A. Back, J. Grun, C. Decker, L.J. Suter, J. Davis, O.L. Landen, R. Wallace, W.W. Hsing, J.M. Laming, U. Feldman, M.C. Miller, and C. Wuest, Phys. Rev. Lett. **87**, 275003 (2001).
- ⁹ D. Babonneau, M. Primout, F. Girard, J.-P. Jadaud, M. Naudy, B. Villette, S. Depierreux, C. Blancard, G. Faussurier, K.B. Fournier, L. Suter, R. Kauffman, S. Glenzer, M.C. Miller, J. Grün, and J. Davis, Phys. Plasmas **15**, 092702 (2008).
- ¹⁰ S. P. Regan, M.A. Barrios, K.B. Fournier, J.D. Kilkenny, J. Emig, C. Bailey, P. Bell, D.K. Bradley, M. Bedzyk, R. Epstein, B.A. Hammel, M.J. Haugh, W. Hising, R. Jungquist, O.L. Landen, D.W. Larson, T. Ma, J. Magoon, D.D. Meyerhofer, M.J. Shoup, L.J. Suter, and D. Rowley, Be Submitt. RSI (n.d.).
- ¹¹ M.J. Haugh, S.P. Regan, K.D. Jacoby, P.W. Ross, J. Magoon, M.A. Barrios, J.A. Emig, M.J. Shoup, and K.B. Fournier, Rev. Sci. Instrum. **83**, 10E122 (2012).
- ¹² B.R. Maddox, H.S. Park, B.A. Remington, N. Izumi, S. Chen, C. Chen, G. Kimminau, Z. Ali, M.J. Haugh, and Q. Ma, Rev. Sci. Instrum. **82**, 023111 (2011).
- ¹³ K.B. Fournier, M.J. May, J.D. Colvin, M.A. Barrios, J.R. Patterson, and S.P. Regan, Phys. Rev. E **88**, 033104 (2013).
- ¹⁴ B.L. Henke, E.M. Gullikson, and J.C. Davis, At. Data Nucl. Data Tables **54**, 181 (1993).
- ¹⁵ F. Girard, M. Primout, B. Villette, P. Stemmler, L. Jacquet, D. Babonneau, and K.B. Fournier, Phys. Plasmas **16**, 052704 (2009).
- ¹⁶ F. Girard, M. Primout, B. Villette, P. Stemmler, L. Jacquet, D. Babonneau, and K.B. Fournier, Phys. Plasmas **18**, 079901 (2011).
- ¹⁷ K.B. Fournier, J.H. Satcher, M.J. May, J.F. Poco, C.M. Sorce, J.D. Colvin, S.B. Hansen, S.A. MacLaren, S.J. Moon, J.F. Davis, F. Girard, B. Villette, M. Primout, D. Babonneau, C.A. Coverdale, and D.E. Beutler, Phys. Plasmas **16**, 052703 (2009).
- ¹⁸ F. Pérez, J.J. Kay, J.R. Patterson, J. Kane, B. Villette, F. Girard, C. Reverdin, M. May, J. Emig, C. Sorce, J. Colvin, S. Gammon, J. Jaquez, J.H. Satcher, and K.B. Fournier, Phys. Plasmas **19**, 083101 (2012).
- ¹⁹ J. Workman and G.A. Kyralla, Rev. Sci. Instrum. **72**, 678 (2001).
- ²⁰ J. Workman and G.A. Kyralla, in (2001), pp. 168–179.
- ²¹ J. Workman, J.R. Fincke, P. Keiter, G.A. Kyralla, T. Pierce, S. Sublett, J.P. Knauer, H. Robey, B. Blue, S.G. Glendinning, and O.L. Landen, Rev. Sci. Instrum. **75**, 3915 (2004).
- ²² F. Girard, J.P. Jadaud, M. Naudy, B. Villette, D. Babonneau, M. Primout, M.C. Miller, R.L. Kauffman, L.J. Suter, J. Grun, and J. Davis, Phys. Plasmas **12**, 092705 (2005).

²³ F. Girard, J.-P. Jadaud, M. Naudy, B. Villette, D. Babonneau, M. Primout, S. Depierreux, M.C. Miller, R.L. Kauffman, L.J. Suter, K.B. Fournier, S.H. Glenzer, C.A. Back, J. Grun, and J.F. Davis, SPIE **5196**, 220 (2004).

²⁴ J. Delettrez, R. Epstein, M.C. Richardson, P.A. Jaanimagi, and B.L. Henke, Phys. Rev. A **36**, 3926 (1987).

²⁵ J.J. MacFarlane, I.E. Golovkin, P. Wang, P.R. Woodruff, and N.A. Pereyra, High Energy Density Phys. **3**, 181 (2007).